Original article

Multi-scale evaluation of mechanical properties of granite under microwave irradiation

Mingzhong Gao[1,2], Yanbo Bai[1]⊙*, Bengao Yang[1], Jing Xie[1], Ruifeng Tang[1], Zundong Yang[1], Yang Zhang[1]

[1]*State Key Laboratory of Intelligent Construction and Healthy Operation and Maintenance of Deep Underground Engineering, College of Water Resource & Hydropower, Sichuan University, Chengdu 610065, P. R. China*

[2]*State Key Laboratory of Intelligent Construction and Healthy Operation and Maintenance of Deep Underground Engineering, Shenzhen University, Shenzhen 518060, P. R. China*

Abstract:
Nowadays, the depletion of shallow resources drives deeper mining operations. Microwave pre-treatment has shown promise for efficient drilling in deep hard rock. While previous studies have confirmed the feasibility of microwave-assisted crushing of hard rocks and analyzed their structural and mechanical property changes at various scales, the microscopic mechanisms behind the evolution of the macro-mechanical parameters of hard rock remain unclear. This study addresses this knowledge gap. At the microscopic scale, the mineral characteristics and the micromechanical properties of minerals (including interfaces) at different sites before and after microwave irradiation were tested in typical hard granites. At the macroscopic scale, the real-time monitoring of mass and surface heating-rupturing characteristics of granite during microwave irradiation was achieved. Meanwhile, acoustic wave and uniaxial compression tests were conducted to explore the evolution of the macroscopic physical and mechanical parameters of granite before and after microwave irradiation. Variability in the mineral structure and mechanical properties accounts for differences in the uniaxial compression strength of granites. To realize the macro-micro linkage, the micro-mechanical parameters of minerals in different granite sections before and after microwave treatment were upscaled. The upscaling results, obtained using the Mori-Tanaka method, closely matched those from uniaxial compression tests, and the upscaling of mineral micro-mechanical parameters in interior samples was found to accurately predict the weakening of macro-mechanical properties of granite. This study provides insights into how microwave irradiation affects the mechanical properties of granite at a microscopic level, offering a quick and efficient method for assessing microwave weakening in deep hard rock and establishing a theoretical foundation for microwave-assisted mechanical drilling in industrial applications.

1. Introduction

Deep hard rock drilling is burdened by several challenges (Xie et al., 2024), including the non-linear increase in rock strength with depth (Yang et al., 2023), leading to high costs from tool wear and limited intrusion depth (Kahraman et al., 2020). Microwave treatment presents a promising solution due to certain advantages, including electronic control, rapid heating, high safety, and cleanliness.

Hard granites frequently pose challenges for underground construction projects (He et al., 2020; Yang et al., 2020). Jerby et al. (2005) developed a microwave drilling apparatus utilizing the thermal runaway phenomenon to weaken non-metallic materials. Hartlieb and Grafe (2017) used Neuhauser granite blocks measuring $50 \times 50 \times 30$ cm^3 to investigate the impact of microwave irradiation on the cutting force of a conical pick in a linear cutting test rig. Rui et al. (2023) developed a numerical virtual platform to simulate the rock disc-cutting problem under microwave irradiation. It was confirmed that

combining microwave and machinery can reduce wear on drill tools, cut construction costs, and boost efficiency.

Subsequently, researchers began to focus on the influence of granite's mineral composition and microstructure on the microwave weakening effect. Rui et al. (2024) concluded that the thermal damage effect in muffle-heated and microwave-heated rocks mainly depends on the fine-grained structure and mineral composition of rocks. Lu et al. (2020) claimed that microwave-induced rock fracture is influenced by the presence of two distinct mineral types: those exhibiting sensitivity to microwaves and those possessing high coefficients of thermal expansion. In a separate study, Law (2014) found that the anisotropy of the thermal expansion coefficient of quartz and the difference in thermal expansion between it and other minerals lead to the formation of lengthwise and through cracks in crystals. From their research, it can be taken forward that the heterogeneity and anisotropy of the coefficient of thermal expansion (CTE) of minerals result in varying degrees of expansion or contraction of particles within during microwave treatment, leading to thermal stress. On the other hand, the heterogeneity of dielectric parameters in minerals causes selective heating under microwave irradiation, yielding different heating rates among mineral particles and the formation of a temperature gradient within the rock, further contributing to thermal stress. When this thermal stress exceeds the strength of the rock, thermal cracking occurs.

However, according to the authors of the above study, the presence of microwave-sensitive minerals and high CTE minerals should not be blamed for the decline in rock strength and cracking damage. For example, as reported by Lu et al. (2020), both Chifeng basalt and Anshan gabbro contain the microwave absorber pyroxene, while the uniaxial compressive strength discount rate of the former is much higher despite minor differences in heating rate. Besides, Nicco et al. (2020) found that strong microwave absorbers are not necessary for cracking and that the microwave response cannot be accurately predicted based on the dielectric constant, color, water, or iron content of the constituent minerals. Furthermore, it is even less appropriate to conjecture about the weakening impact of rocks based on the presence of high CTE minerals, since the thermal expansion of minerals is likely to facilitate the closure of pre-existing microcracks and pores, which was also categorized by Wong et al. (2020) as one of the important mechanisms of rock heating enhancement. Overall, it is complicated and challenging to accurately predict the weakening-fracturing effect of rocks based on electromagnetic-thermophysical parameters of rock-forming minerals. Instead, deciphering the evolution patterns of mechanical properties of hard-rock rock-forming minerals under microwave action is more pertinent to this task.

Traditional macro-mechanical testing suffers from the following defects, as analyzed by Lei (2022): (1) the difficulty and high cost of sampling and processing; (2) the inability to perform other tests after cores are destroyed; (3) the high dispersion of test results; and (4) the failure to consider the effect of mineralogical composition on the macroscopic mechanical properties. Hence, the authors of this study used the nanoindentation test with higher test resolution to rapidly assess the mechanical properties of the mineral components in samples before and after microwave irradiation. A significant advantage is that nanoindentation enables the evaluation of mechanical properties in various regions of rocks, as the interior temperature of rocks tends to be higher after microwave heating.

To effectively elucidate the micro-mechanisms underlying variations in the macro-mechanical parameters, the implementation of a multi-scale mechanical approach is essential. The current research on scaling up rock material properties can be categorized into three groups: (1) directly considering the average of mechanical properties from a significant number of nanoindentation test results as macroscopic properties (Espinoza et al., 2022); (2) utilizing data from numerous nanoindentation tests, the intricate mineral composition of rocks is simplified into several mineral clusters via the inverse folding method. Subsequently, the micro-scale characteristics of these mineral clusters are upscaled to the macroscopic level through homogenization calculations (Róański et al., 2021); (3) integrating nanoindentation with advanced imaging methods like Backscattered Electron Detector/Energy Dispersive Spectrometer for the determination of micro-mechanical characteristics of targeted minerals, and then combining the measured mineral content for homogenization calculations (Ma et al., 2022). For category (1) studies, since the non-homogeneity and anisotropy of rock materials are not fully considered, there is a large discrepancy between the arithmetic mean of micro-modulus and the macro-modulus. Research in categories (2) and (3) is relatively scarce. By comparing the upscaling results with those of conventional macro-mechanical experiments, it was found that some of the results were in good agreement with the actual parameters (Ma et al., 2022; Liu et al., 2023), while others differed from the actual ones (Li et al., 2021). Lei (2022) claimed that there were differences in the morphologies, spatial arrangements, and bonding characteristics of mineral particles in granites with the calculation assumptions made by the various upscaling methods, which are considered to be the sources of upscaling errors. Fortunately, Li et al. (2021) found that method (3) was more accurate. This is because the deconvolution method operates under the assumption that the mechanical properties of mineral clusters adhere to a normal distribution, thereby introducing additional uncertainty in the findings. It follows that method (3) can minimize the scale-up error.

To sum up, in this paper, by combining X-Ray Diffraction (XRD), Scanning Electron Microscope-Energy Dispersive Spectrometer (SEM-EDS) and the nanoindentation test, the mineral composition content of granites and the micro-mechanical properties of the mineral crystals in different parts of granites before and after microwave irradiation were accurately tested. The developed deep hard rock microwave-assisted drilling test system was used to monitor the mass variation and heating and fracturing characteristics of granites under microwave irradiation in real-time. The P-wave velocity test and uniaxial compression test were implemented to analyze the macroscopic physical and mechanical properties of granites both before and after exposure to microwave irradiation. Finally, the micromechanical parameters of minerals in various regions of the granites were upscaled to facilitate

the comparison of results obtained from the uniaxial compression test. The optimal calculation method for scaling up granite samples pre- and post-microwave irradiation, as well as the most appropriate nanoindentation sampling location, were determined. This research delves into the microscopic mechanisms underlying changes in macroscopic mechanical properties of granite following microwave irradiation, advancing the theoretical and experimental groundwork for the industrial utilization of microwave-assisted mechanical drilling in hard rock formations.

2. Experimental equipment and protocols

2.1 Sample preparation and component test

Typical hard granite was taken from the Guoluo Tibetan Autonomous Prefecture, Qinghai Province, China, and designated as granite B. The specific experimental procedure is shown in Fig. 1, prescribed by the International Society for Rock Mechanics, six granite specimens (three for uniaxial compression testing and three for testing after microwave treatment followed by uniaxial compression) were fabricated into standard cylinders measuring 100 mm in height and 50 mm in diameter. Before irradiation, the granite samples must be dried in an oven at 110 °C for 24 hours. Three nanoindentation samples of granite B were extracted from any location within the untreated sample and from both the outer surface and interior regions of the microwave-treated sample. An $8 \times 8 \times 4$ mm^3 square sheet (with a thickness significantly greater than 10 times the h_{max}) of granite was initially cut from samples using a Struers cutter. Subsequently, the surface of the samples underwent a sequential grinding process utilizing sandpaper with grits of P320, P600, and P1200, with each grit used for a grinding time exceeding 30 minutes. Subsequently, the samples were sequentially polished with polishing cloths of 6, 3, 1, and 0.05 μm diamond slurry, with anhydrous ethanol utilized for cleaning during the polishing procedure. Finally, the samples were placed in an oven at 50 °C for 24-48 h until completely dry. The mineral content of granite B was determined by XRD. The results revealed that granite B contained 15% quartz (Q), 10% alkali feldspars (Afs, with a predominant presence of K-feldspar in thin sections), 62% plagioclase (Pl), and 13% biotite (Bit).

2.2 Experimental equipment and parameters

The microwave irradiation granite test was carried out using the deep hard rock microwave-assisted drilling test system independently developed by Sichuan University, with the microwave irradiation section shown in Fig. 1. The system operates at a frequency of 2.45 GHz, irradiating hard granites with a 2 kW microwave for 3 minutes. Simultaneously, the device's integrated thermogravimetric monitoring module, infrared thermal imaging module, and high-definition camera module captures real-time data on the mass changes, heating patterns, and damage characteristics of the hard rocks.

The GCTS Rock Comprehensive Test System, sourced from Sichuan University, was employed for the experiment. Regarding the macro-mechanics experimental section depicted in Fig. 1, the present study focused on conducting uniaxial compression tests to acquire macro-mechanical parameters. The sample was initially subjected to a preloading rate of 0.05 kN/s with a pre-pressure of 0.5 MPa. Subsequently, the deformation control mode was utilized to prevent the excessive collapse of the granite specimens. The axial loading rate was established at 0.04 mm/min, and the axial and circumferential deformations of the specimen during loading were monitored using axial displacement transducers and circumferential displacement transducers.

The different minerals' distribution areas are recognised based on their elemental distribution characteristics. For instance, in regions devoid of Al, Q exhibited the highest Si enrichment, while the overlap of Al-enriched and K-enriched areas was observed in Afs. Additionally, Pl demonstrated higher Ca and Na enrichment in Al-enriched regions, whereas Bit exhibited elevated levels of Mg and Fe enrichment in the same areas.

A Berkovich indenter was employed to perform nanoindentation testing using the micro-material nanoindentation test system within the micro-mechanics experimental section depicted in Fig. 1. In combination with the optical microscope integrated with the nanoindentation system, nanoindentation tests were carried out on specific mineral interiors and interfaces by positioning the SEM-EDS scanning area. The nanoindentation test was carried out in load-controlled mode with a peak load of 80 mN, a holding time of 10 s, and a loading and unloading rate of 2 mN/s. In consideration of the disparities in histological heterogeneity and surface roughness among the minerals, 2-3 sites featuring flat and smooth surfaces were chosen for the nanoindentation experiments, with a total of 12 indentations per mineral or interface. To allow the plastic deformation zone within the material to expand uniformly (ISO 14577-1, 2003), the indentation spacing was set as 10 or 20 μm in this study.

2.3 Test principle and typical curve

Based on the analysis of axial stress-strain curve of specimens, the macro-mechanics experimental process depicted in Fig. 1 can be divided into five distinct stages (Brady and Brown, 2007): crack closure stage, elastic deformation stage, crack initiation and stable expansion stage, crack unstable expansion stage, and post-peak deformation stage. Meanwhile, nanoindentation is characterized by three primary stages: loading, holding, and unloading. The details of these three stages are referred to the study by Ma et al. (2020).

3. Results and discussion

3.1 Impacts of microwave irradiation on mass and P-wave velocity

Since the granite samples were completely dried at 110 °C prior to microwave irradiation, the evaporation of adherent moisture was no longer considered. As shown in Fig. 2, the mass change trend of granite B in the microwave field decreases slowly from 0 to 90 s and accelerates from 90 to 180 s. The mass of granite B decreases by 0.47 g after heating, which may be related to its heating pattern. Comparing the
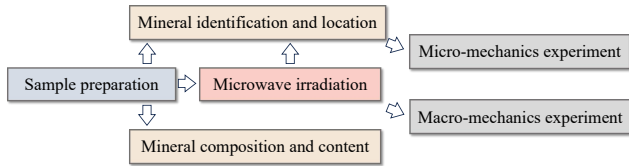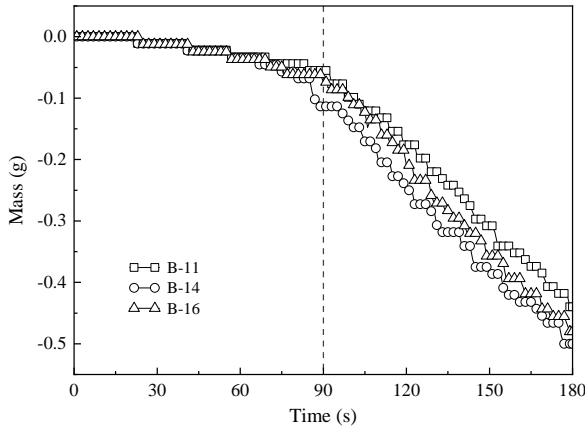
Fig. 1. Experimental procedure.

Fig. 2. Changes in the quality of granite B under microwave irradiation.

temperature change curves of granite B shown in Fig. 3, its maximum surface temperature exceeds 200 °C near 90 s; at 180 s, the maximum surface temperature of granite B reaches 300 °C. From these data, it can be surmised that the main reason for the accelerated mass loss from 90 to 180 s is the overflow of bound, microporous and structural water inside the minerals (Wong et al., 2020). Meanwhile, after 3 min of microwave heating at 2 kW, the average P-wave velocity of granite B decreases from 5.143 to 4.024 km/s, with a discount rate of 21.76%. This proves that microwave heating leads to the multiplication of internal defects in granite.

3.2 Impacts of microwave irradiation on surface heating rupture behavior

The granite used in this study is a weak microwave absorber. Its average heating rate is slow at only 1.32 °C/s. As shown in Fig. 3, in terms of maximum temperature, the growth rate is faster during 0-50 s, then it decreases and tends to change at a uniform rate. The authors suggest that this heating trend is typical for microwave-sensitive minerals, such as the biotite and pyroxene minerals studied by Lu et al. (2017), where the heating rate is first rapid and then slows down. However, in granite B, this phased progression is relatively insignificant. The main reason is that there are other insensitive minerals in this type of granite, and heat will be transferred to the surrounding minerals after the formation of a locally high temperature zone. Meanwhile, the average temperature change of granite B shows a linear trend, which has also been found in other studies (Lu et al., 2020).

Due to the non-uniformity of the microwave field and the non-homogeneity of granite, the surface temperature distribu-
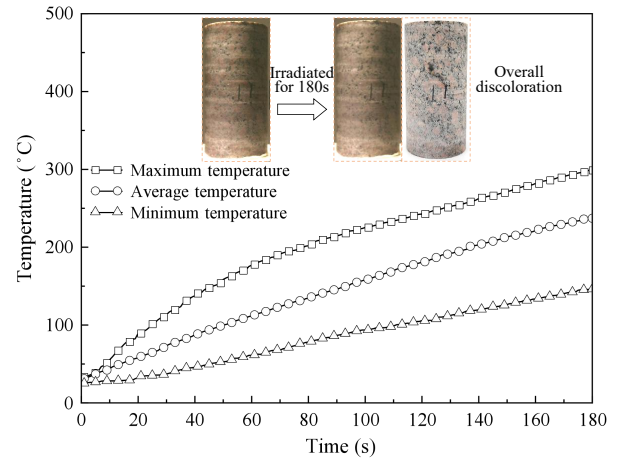

Fig. 3. Temperature curves and fracture characteristics of granite B surface under microwave irradiation.
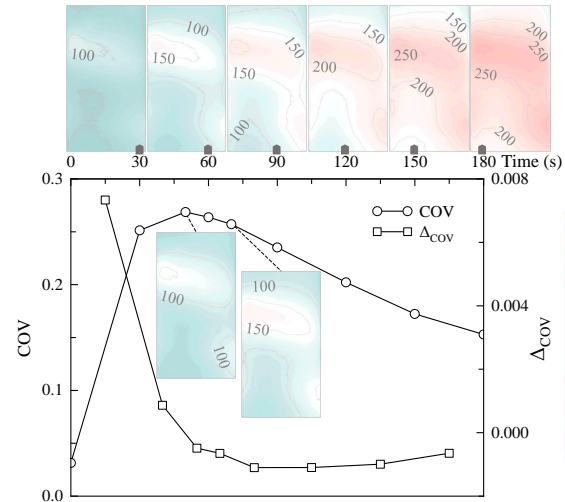

Fig. 4. Variation in surface temperature distribution and COV of granite B under microwave irradiation.

tion in granite B is consistently inhomogeneous. As shown in Fig. 4, a large local high-temperature region in the upper part of the sample surface of granite B initially forms and simultaneously a small high-temperature region in the lower right part. With the progress of microwave irradiation time, the high-temperature region gradually expands in all directions, and the uniformity of the surface temperature distribution gradually increases. To further quantify the uniformity of the surface temperature distribution, the coefficients of variation (COV) and $\triangle_{COV}$ were introduced. As shown in Fig. 4, the COV value of B reaches a maximum of 0.27 at 50 s, and then gradually decreases and stabilizes. The turning point of the COV and the slope turning point of the maximum temperature are both located at 50 s. Correspondingly, the value of $\triangle_{COV}$ is largest at the beginning, then decreases rapidly to a negative value, and eventually increases slowly, tending to 0. This indicates that the dispersion of the surface temperatures of B increases from 0 to 50 s, and then decreases gradually before stabilizing. As illustrated in Fig. 3, the surface morphology of B is less variable. Only the overall color of its surface is altered
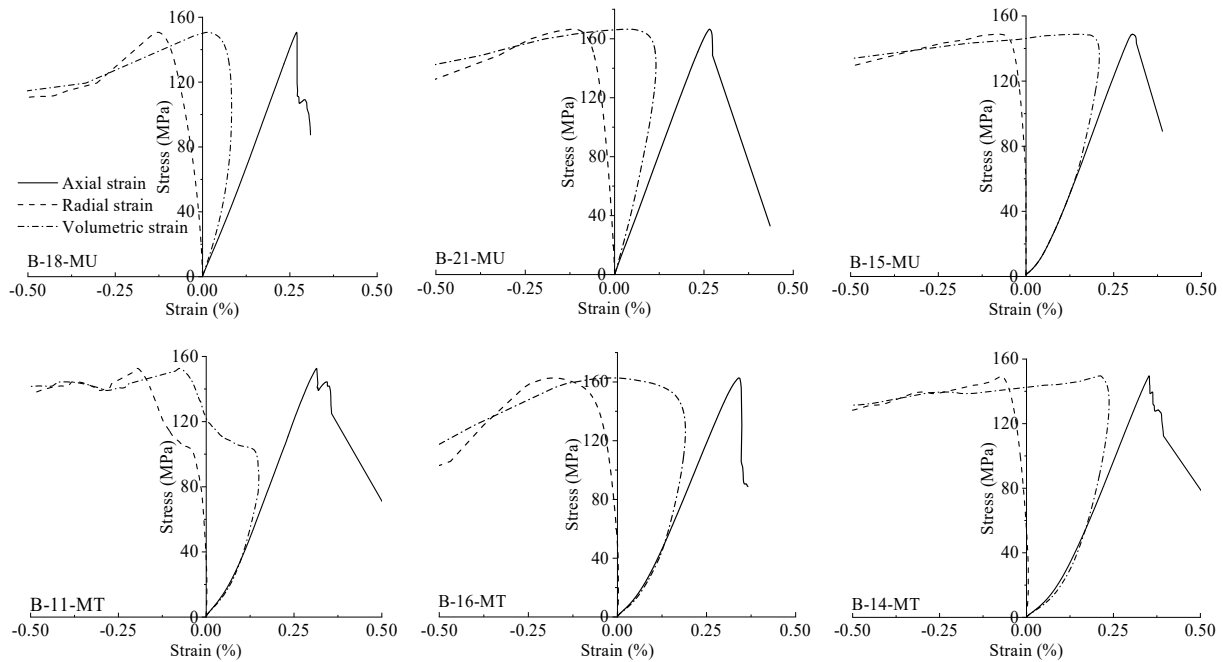
Fig. 5. Uniaxial compression curves and damage forms in granite B before and after microwave irradiation (MU-Microwave Untreated, MT-Microwave Treated).

upon heating. According to the authors' observations of rock-thin sections, most of the mineral grains in B are between 0.2 and 2 mm in size. According to Nicco et al. (2018), this small-grained rock tends to form a small number of wide cracks under microwave irradiation.

3.3 Impacts of microwave irradiation on macro-mechanical properties

3.3.1 Uniaxial damage forms

Before microwave irradiation, the rock exhibits shear damage, which includes uniaxial oblique shear damage shown in B-21 and X-shaped conjugate oblique shear damage shown in B-18. On the other hand, the untreated sample exhibits violent damage under uniaxial compression, accompanied by a large number of spalled fragments of different volumes. After 3 min of microwave heating at 2 kW, the intensity of the uniaxial compression damage of the rocks decreases, with the exfoliation of small particles of rock fragments and fine particles of rock dust. In addition, the structural integrity of the microwave-treated uniaxial compression specimens is higher, and the fracture of the rocks is mainly caused by axial cracks, which is an obvious characteristic of tensile damage.

With respect to the damage mechanism, the damage mode of granite B under uniaxial compression evolves from shear to tensile damage after microwave heating. A similar phenomenon was found by Su et al. (2023). The decrease in damage intensity, the increase in samples' structural integrity, and the decrease in rock chip volume and number confirm that the brittleness of granite has decreased after microwave treatment. Notably, the microwave-treated rocks showed flank fracture damage similar to "compression rod instability". You

and Hua (1998) explained that when the initial shear slip surface occurs inside the sample, the resulting axial tensile cleavage surface may cause the rock flank material to detach from the main body and become a compression bar, which bends, destabilizes, and eventually breaks under pressure. A similar curvilinear phenomenon described by You and Hua (1998) was also found in this study, i.e., a small drop in stress and almost constant strain near the peak intensity, as shown in B-11 in Fig. 5. However, similar phenomena were not found in the untreated samples.

3.3.2 Uniaxial compression curves

The period of the crack closure stage of granite was significantly longer after microwave treatment, as seen in Fig. 5. This indicates that the microwave action resulted in more microcracks in the granite, which is also proved by the decrease in the P-wave velocity of granite B in Section 3.1. Meanwhile, the small increase in the circumferential strain curve at the initial stage likewise indicates that the micro-defects of the treated samples take a longer time to be compressed and closed. Furthermore, during the post-peak deformation stage, the stress-strain curves of the untreated samples decreased rapidly after reaching the peak value. However, due to the reduced brittleness of the granites, the sudden stress drop of the microwave-treated samples was weakened and was able to show some post-peak, as shown in B-11 and B-14 of Fig. 5.

3.3.3 Macro-mechanical parameters

The peak strength, peak strain, elastic modulus and Poisson's ratio of granite B before and after microwave irradiation were obtained from the stress-strain curves of the uniaxial compression tests. As shown in Figs. 6(c)-6(d), both elastic
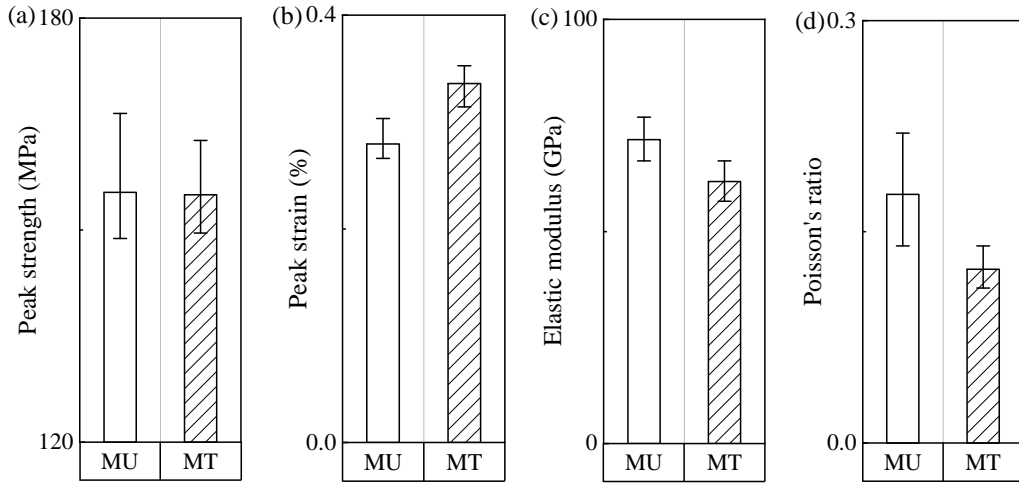
Fig. 6. Variation in the macro-mechanical parameters in granite B after microwave irradiation: (a) Peak strength, (b) peak strain, (c) elastic modulus and (d) poisson's ratio (the detailed formulas for elastic modulus and poisson's ratio are presented in Appendix A).
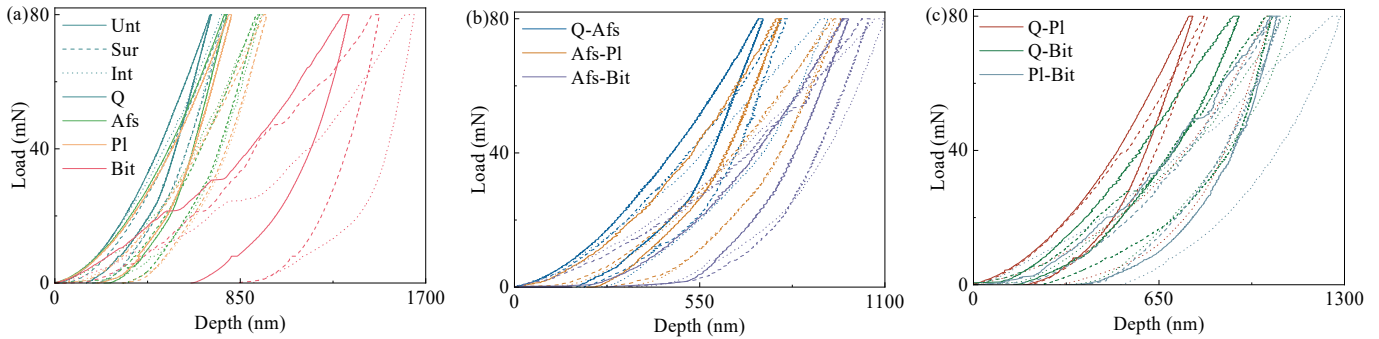

Fig. 7. Load-depth curves of mineral crystal interiors and interfaces in different parts of granite B before and after microwave irradiation: (a) Mineral crystal interiors (Unt-Untreated sample, Sur-Surface sample, Int-Interior sample), (b) mineral crystal interfaces (Q-Afs, Afs-Pl, Afs-Bit) and (c) mineral crystal interfaces (Q-Pl, Q-Bit, Pl-Bit).

modulus and Poisson's ratio of granite B decreases after microwave irradiation, with discount rates of 13.73% and 25.81%, respectively. As depicted in Figs. 6(a)-6(b), the peak strain of B increases by 20.18%, which is related to the increase of micro-defects in the constituent minerals and the discounting of strength after microwave heating, leading to the gradual accumulation of plastic strain and a decrease in the brittleness of granites. Anomalously, there is little change in the peak strength of granite B, with only a minor decline of 0.21%. This may be because the thermal expansion of the minerals promotes the closure of pre-existing microcracks and pores (Wong et al., 2020).

3.4 Impacts of microwave irradiation on micro-mechanical properties

3.4.1 Load-depth curves

One representative load-depth curve for different parts of minerals and mineral interfaces in granite B before and after microwave irradiation was selected for comparison and analysis. The known hardness was defined as the maximum load applied perpendicular to each unit of contact area (Oliver and Pharr, 1992). From this, it can be surmised that the indentation depth of the sample (the maximum depth of the loading stage) is also negatively correlated with its hardness. As shown in Figs. 7 and 8, for the minerals of B, Q has the smallest indentation depths of 717.62 mm (note that all parameters in the subsequent section are by default the average of multiple measurements). This is followed by Afs and Pl, with indentation depths generally in the range of 730-830 mm. Among these, Afs has a smaller indentation depth and a harder texture. Bit is the most deformed mineral, with an indentation depth in the range of 1,200-1,400 nm, suggesting that it has the softest texture. Meanwhile, the early indentation depth of Bit increases at an extremely fast rate, which was considered to be compacted along the normal solution direction by Liu et al. (2023). For the mineral boundaries of granite B, the indentation depths, from smallest to largest, are in the order of: $D_{Q-Afs} < D_{Q-Pl} < D_{Afs-Pl} < D_{Q-Bit} < D_{Afs-Bit} < D_{Pl-Bit}$. Specifically, the indentation depth at the junction of two
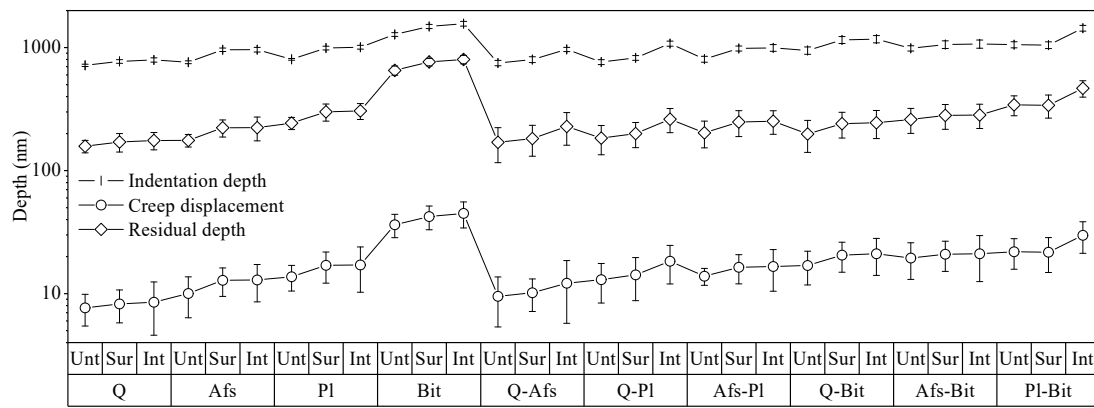
Fig. 8. Variation in the indentation depth, creep displacement and residual depth of minerals and mineral interfaces in different parts of granite B before and after microwave irradiation.

minerals may be between the indentation depth values of the two minerals or greater than the indentation depth value of the mineral with the greater indentation depth. Because the direction of boundary extension hardly ever coincides with the indentation direction of the indenter, there is always one mineral whose mechanical properties have a greater impact on the test results.

After microwave irradiation, an increase in the indentation depth of both minerals and mineral interfaces occurred in B, implying a decrease in the strength of both minerals and mineral interfaces. For the minerals in the surface sample, Afs and Pl showed the highest increase in indentation depths of 26.40% and 23.64%, respectively, which Nicco et al. (2020) attributed to the cracking of brittle particles of feldspars along the disintegrated surfaces due to thermal expansion. The mineral Q, which demonstrated the worst microwave sensitivity, had the least indentation depth increment of only 7.57%. Bit exhibited an indentation depth increment of only 16.22%, but its microwave absorption capacity is significantly stronger than that of feldspar minerals. This means that the microwave absorption capacity of minerals cannot act as a standard to quantify their weakening effect. As far as the mineral interfaces of the surface sample are concerned, the largest increases in indentation depths were found in Afs-Pl and Q-Bit, at 22.86% and 21.81%, respectively. If the large increment in indentation depth for Afs-Pl can be attributed to the large strength discounting of both feldspars, the large increment in indentation depth for Q-Bit is an entirely distinct mechanism. The authors attribute this to the high thermal expansion nature of Q and Bit, for which Nicco et al. (2020) make a similar point. In addition, the indentation depth of Pl-Bit was almost constant, with incremental indentation depths in the range of 6%-8% for the remaining boundaries. It is interesting to note that the indentation depth increased more at the minerals and mineral interfaces of sample inside granite B. This is most likely due to the higher interior temperature of the sample after microwave heating, resulting in a better weakening effect of the mechanical properties of the interior minerals and their interfaces. The indentation depth increment of Bit reached 22.42%, while the increment of the rest of minerals was less compared to the surface sample. The

indentation depth increment of Q-Afs, Q-Pl and Pl-Bit reached 30%-40%. Meanwhile, the indentation depth increment of Afs-Pl, Q-Bit, and Afs-Bit, however, was very limited at only 1%-2% compared to their indentation depths in the surface sample. The authors suggest that if the limited improvement in Afs-Pl is attributed to the poorer thermal expansion properties of feldspars, then the limited improvement in indentation depths for Q-Bit and Afs-Bit needs to be considered in the anisotropic nature of the thermal expansions for Q and Bit. On the other hand, since Bit has complete resolution, cracks may propagate in the Bit band by connecting the resolution surfaces instead of propagating along the boundary of Bit (Nicco et al., 2020).

Creep displacement is the most direct parameter to describe the creep behavior of different minerals and mineral interfaces (Ma et al., 2022). As illustrated in Figs. 7 and 8, the creep displacements of granite B minerals are arranged, from largest to smallest, as follows: $L_Q < L_{Afs} < L_{Pl} < L_{Bit}$, which is consistent with the ordering of their indentation depths. In addition, the creep displacements at the mineral interfaces of B exhibit the same patterns, which implies that the creep displacements of minerals and mineral interfaces are also negatively correlated with hardness. As indicated in Figs. 7 and 8, another item that has a similar pattern of change with the indentation depth is the residual depth at minerals and mineral interfaces, which findings are similar to those in Lei et al. (2021) and Liu et al. (2022). These data show that hard minerals have better elastic recovery and soft minerals have better plastic deformation. Similarly, the plastic deformation capacity of granite minerals and mineral interfaces after microwave treatment again shifted according to their hardness.

In addition, for Q, Afs, Pl and their corresponding mineral interfaces, the load-depth curves were smoother and the loading process was steeper. On the other hand, as shown in Fig. 7, the indentation depth of Bit and its corresponding mineral interfaces increases sharply in the early part of the loading stage and the curve slope increases slowly in the late part, which also leads to its higher indentation depth. Another reason for the higher indentation depths is the large number of "pop-in" events in the curves of the Bit and its corresponding mineral interfaces. This high frequency of "pop-
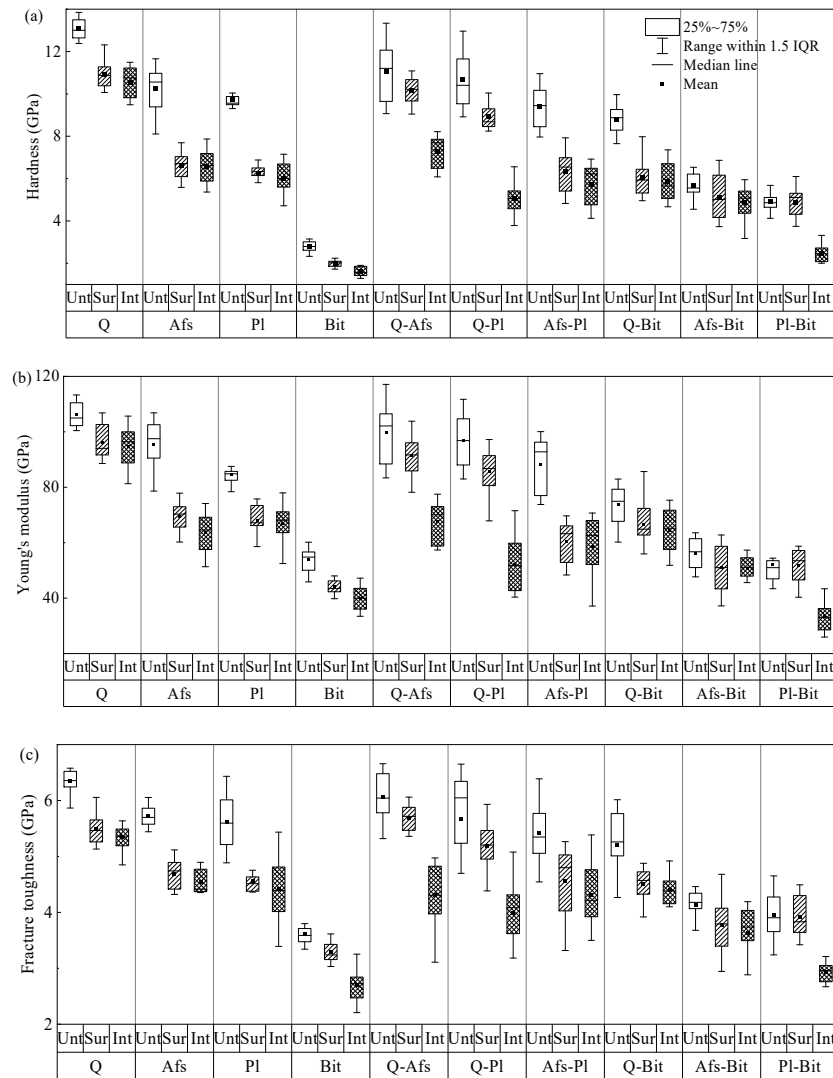
Fig. 9. Variation in the hardness, Young's modulus and fracture toughness of minerals and mineral interfaces in different parts of granite B before and after microwave irradiation (the detailed calculation procedures for hardness, Young's modulus and fracture toughness are presented in Appendices 2 and 3): (a) Hardness, (b)Young's modulus and (c) fracture toughness.

in" events may be related to the instability of the layered microstructure of Bit (Liu et al., 2022), which Zhang et al. (2013) attributed to the generation of kink bands and layering in Bit. Besides, the "pop-in" events in Bit and its corresponding mineral interfaces are much larger in terms of displacement. This is due to the weaker interactions, larger interlayer spacing and the presence of water molecules in Bit before microwave heating (Mukherjee and Misra, 2023). At the same time, since the indentation depth is much larger than the layer spacing of Bit, more "pop-in" events occur due to the crack generation and extension caused by the indenter penetration into the disintegrated surface during the pressing stage. After microwave treatment, the loading curve was gradually smoothed, which is likely attributed to the evaporation of water molecules in Bit and its rapid shrinkage along the direction perpendicular to the laminae.

3.4.2 Hardness and Young's modulus

The hardness of minerals of granite B before microwave irradiation is illustrated in Fig. 9(a). According to the test results of other scholars, the hardness ranges of Q, Afs, Pl, and Bit are 9.3-14.5 GPa (Zhu et al., 2007; Liu et al., 2023; Mukherjee and Misra, 2023), 7.5-11.4 GPa (Sousa et al., 2014; Maruvanchery and Kim, 2020; Liu et al., 2023), 3.2-9.0 GPa (Maruvanchery and Kim, 2020; Meng, 2022; Liu et al., 2023) and 1.5-3.3 GPa (Zhang et al., 2013; Liu et al., 2023), respectively. This justifies the test results of different minerals in this paper. The hardnesses of corresponding mineral interfaces in granite B are exhibited in Fig. 9(a). The only measurements of hardness at granite mineral interfaces were made by Liu et al. (2023), who determined the hardnesses of Q-Kfs (Kfs is K-feldspar), Q-Pl, Kfs-Pl, Q-Bit, and Kfs-Bit as 12.1, 8.2, 2.5, 2.8, and 3.6 GPa, respectively. Their results are significantly different from the test values established in this study, thus showing

that the variability of the mechanical properties of the same mineral boundaries in different rocks is stronger than that of the minerals within. Of note, when the minerals on one side are the same, the mechanical properties of the mineral interfaces do not necessarily depend on those of the minerals on the other side, e.g., Q-Bit and Kfs-Bit in the granite tested in Liu et al. (2023).

After microwave irradiation, for the minerals in the surface sample of granite B, the hardness of Afs and Pl decreased the most after microwave irradiation, reaching about 35%, as shown in Fig. 9(a). This was followed by Bit, and the hardness of Q was reduced by only 16.37%. Certainly, the hardness of minerals in the interior sample of B was reduced more, and that of Afs, Pl and Bit was reduced by about 40%, whereas the hardness of Q was reduced by only 19.20%. This once again demonstrates that there is no absolute correlation between the weakening effect of microwaves on granite-forming minerals and the microwave sensitivity of rock-forming minerals. On the other hand, for the mineral interfaces in the surface sample of granite B, the hardness decreased by more than 30% for Afs-Pl and Q-Bit. The hardnesses of Q-Afs, Q-Pl, and Afs-Bit decreased by about 10%, and that of Pl-Bit remained almost unchanged. The decrease in the hardness of the mineral interfaces of the interior sample compared to the surface sample varied, with Q-Afs, Q-Pl and Pl-Bit showing a larger decrease of more than 25%, and Afs-Pl, Q-Bit and Afs-Bit showing a decline of only about 5%.

The ranking of the Young's modulus of granite B before microwave irradiation, shown in Fig. 9(b), is consistent with their hardness and indentation depth. According to the test results of other scholars, the Young's modulus ranges of Q, Afs, Pl, and Bit are 55-124 GPa (Broz et al., 2006; Zhu et al., 2007), 62.0-100.6 GPa (Zhu et al., 2007; Sousa et al., 2014; Liu et al., 2023), 44.0-88.1 GPa (Swan, 1978; Zhu et al., 2007; Maruvanchery and Kim, 2020), and 37.1-68.3 GPa (Swan, 1978; Tang et al., 2022), respectively. Apparently, our test data fell within these ranges, further confirming its validity. On the other hand, the Young's modulus of the corresponding mineral interfaces in granite B is displayed in Fig. 9(b). For comparison, the Young's modulus of Q-Kfs, Q-Pl, Kfs-Pl, Q-Bit, and Kfs-Bit tested by Liu et al. (2023) were 91.6, 71.4, 57.4, 56.0, and 56.4 GPa, respectively, showing a deviation from our test data from the mineral interfaces of granite B. The authors argued that the surround and base effects at the mineral interfaces, coupled with the non-homogeneity of defect density and fine-scale structure, resulted in much greater variability in the test data at the mineral interfaces than within the minerals; similar conclusions were drawn by Liu et al. (2023). Another noteworthy phenomenon is that the standard deviation of the mineral interfaces of B was much larger, further illustrating the greater variability of the mineral interface test data. Meanwhile, the standard deviation of the minerals and mineral interfaces data did not show a strict increasing or decreasing pattern due to microwaves.

After microwave irradiation, for the minerals in the surface sample of granite B, the Young's modulus folding rate of Q was only 9.43%, followed by Bit and Pl with 18.48% and 19.41%, respectively, and Afs showing the best weakening effect of 27.21%. In addition, the weakening effect was better for the interior sample compared to the surface sample. However, the weakening effect of quartz and feldspar minerals only increased by 1%-2% and that of Bit by 7.89%. The mineral interfaces of the surface sample demonstrated the best weakening effect of 31.48% for Afs-Pl. The Young's modulus of Q-Afs, Q-Pl, Q-Bit, and Afs-Bit was only discounted by about 10%, and the Young's modulus of Pl-Bit changed very little. There was a difference between the Young's modulus and the hardness of individual interfaces, e.g., the weakening of the hardness of Q-Bit was better, but the weakening of its Young's modulus was average. The weakening effect of mineral interfaces in the interior sample was enhanced to different degrees, which is consistent with the change patterns of hardness, and the weakening effect of Q-Afs, Q-Pl and Pl-Bit was significantly enhanced to 20%-30%, while the weakening effect of Afs-Pl, Q-Bit and Afs-Bit was only enhanced by 1%-3%.

3.4.3 Fracture toughness

The test results for fracture toughness in this study also show many similar patterns with those for Young's modulus, which are shown in Fig. 9(c). According to the test results of other scholars (Meng, 2022; Liu et al., 2023), the fracture toughness ranges of Q, Afs, Pl, and Bit are 4.30-5.41, 4.06-4.99, 2.70-3.30, and 2.12-3.25 GPa, respectively. Obviously, our test data differ considerably from these results, whereas the current test data for mineral fracture toughness are extremely limited, justifying the value of this study. The fracture toughness of corresponding mineral interfaces in granite B is also demonstrated in Fig. 9(c), while the fracture toughness of Q-Kfs, Q-Pl, Kfs-Pl, Q-Bit, and Kfs-Bit tested by Liu et al. (2023) were 4.96, 4.00, 2.55, 2.59, and 2.85 GPa, respectively. Apparently, the latter test results are all lower than those for granite B. In other words, there is some discrepancy between this and the test data for the mineral interfaces of granite B. This can be attributed to two factors: on the one hand, differences in sampling areas and diagenetic history; on the other hand, differences in mineral crystal systems and effect of mineral anisotropy.

After microwave irradiation, for the minerals of granite B, the weakening effect of fracture toughness was the best for Afs and Pl in the surface sample, reaching 18.01% and 19.04%, respectively. The discount rate was lower for Q and Bit at only 13.54% and 8.86%, respectively. Meanwhile, in the interior sample, the discount rate increased by only about 2% for Q, Afs and Pl, but increased by 16.34% for Bit. This may be a pattern specific to Bit, as a similar pattern can be seen in parameters such as hardness, Young's modulus and indentation depth. For the mineral interfaces of granite B, in the surface sample, the fracture toughness of Afs-Pl and Q-Bit, which were weakened to a greater extent, decreased by 15.68% and 13.27%, respectively. The discount rates of Q-Afs, Q-Pl, and Afs-Bit were in the range of 5%-10%, with the worst weakening effect in the case of Pl-Bit, while in the interior sample, the weakening effect of minerals was better. Compared to the surface sample, the weakening effect of Q-Afs, Q-Pl, and Pl-Bit was enhanced by 20%-25%, while the
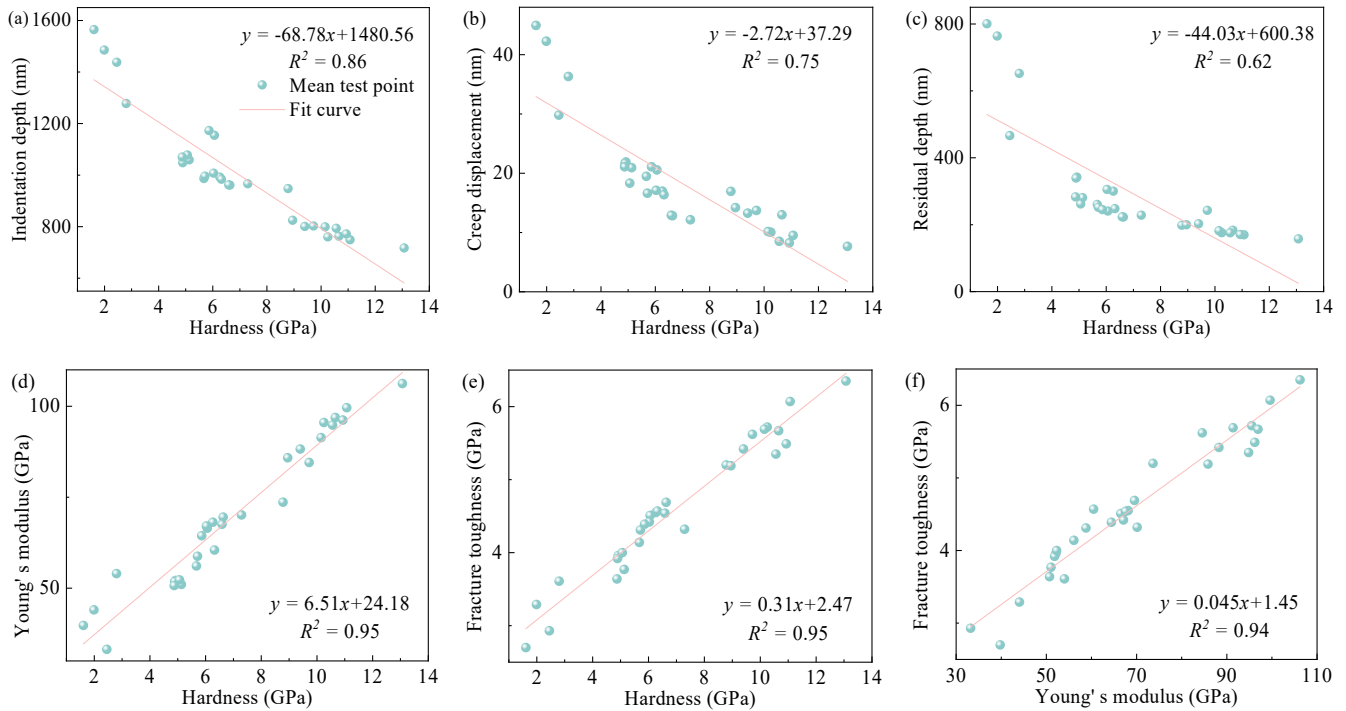
Fig. 10. Correlation between the micromechanical parameters of granite B: (a) Indentation depth and hardness, (b) creep displacement and hardness, (c) residual depth and hardness, (d) Young's modulus and hardness, (e) fracture toughness and hardness and (f) fracture toughness and Young's modulus.

enhancement of discount rate for Afs-Pl, Q-Bit, and Afs-Bit was only 2%-5%. This is similar to the evolution pattern of its hardness, Young's modulus and indentation depth.

4. Discussion

4.1 Correlation analysis of micro-mechanical parameters

The determination of various micro-mechanical properties of the samples will be more convenient if the relationship between two micro-mechanical parameters can be expressed. Therefore, the authors analyzed the relationship between hardness, Young's modulus and fracture toughness using least squares linear regression, as well as the relationship between hardness and Young's modulus, indentation depth, creep displacement, and residual depth. Thirty data points were taken from each sample. As shown in Fig. 10(a), the linear correlation between indentation depth and hardness before and after microwave action is favorable, with a coefficient of determination, R^2, of 0.86. This is because hardness is directly correlated with the contact area, i.e., the depth of contact, when the maximum load is constant. Meanwhile, the contact depth is positively correlated with the maximum indentation depth, i.e., with the loading depth. The reason for this is that the creep displacement is in the order of nanometres while the indentation depth is close to the order of micrometers, so the effect of the difference in the creep deformation increment on the relationship between indentation depth and hardness can be neglected (Espinoza et al., 2022). As a result, the indentation

depth and hardness show a strong negative linear correlation.

In addition, the correlation between hardness and creep displacement before and after microwave irradiation is positive, with a coefficient of determination of 0.75 as shown in Fig. 10(b). Espinoza et al. (2022) also tested the relationship between creep displacement versus hardness and Young's modulus at different temperatures and found that creep displacement showed a linear relationship with hardness. This further suggests that hardness can be a candidate for preliminary assessment of the creep deformation of rocks or minerals under a microwave effect. The correlations of hardness versus creep displacement and hardness versus residual depth are poorer than those of hardness versus indentation depth. Among them, the coefficient of determination of hardness versus residual depth is merely 0.62, as shown in Figs. 10(b)-10(c). The authors believe that it is mainly affected by the Bit laminar structure. Specifically, the pop-in events caused by the indenter penetrating the laminae during load-holding would bias the creep displacement, while the unrecoverable nature of the destroyed laminae during unloading would bias the residual depth.

On the other hand, an excellent correlation between hardness and Young's modulus is evident with a coefficient of determination of 0.95, as shown in Fig. 10(d). Ante et al. (2018) also found a positive correlation between hardness and Young's modulus of rocks. As seen in Fig. 10(e), before and after microwave irradiation, fracture toughness positively correlates with hardness, and the coefficient of determination is also as high as 0.95. Other scholars have reached similar
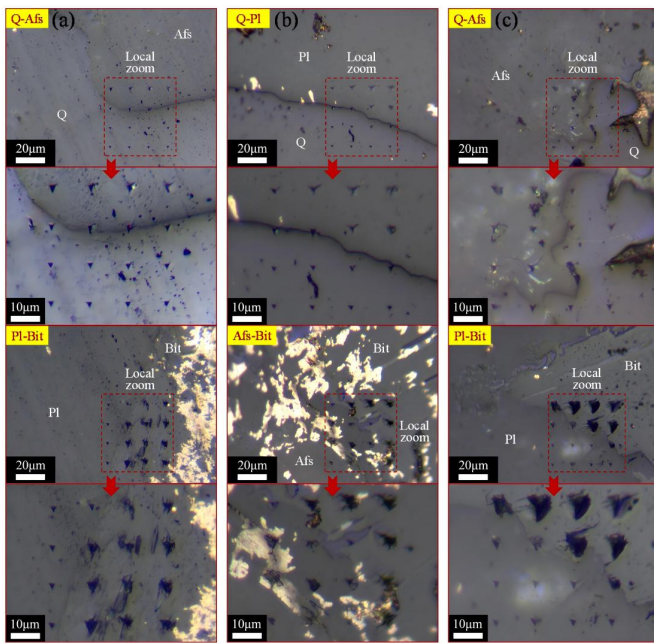
Fig. 11. Variation in the indentation morphology of minerals in different parts of granite B before and after microwave irradiation: (a) B-Unt, (b) B-Sur and (c) B-Int.

conclusions (Ma et al., 2022; Chen et al., 2023). As illustrated in Fig. 10(f), the correlation between fracture toughness and Young's modulus is also excellent, with the coefficient of determination reaching 0.94. Unlike Chen et al. (2023) who concluded that it is better to use Young's modulus to predict fracture toughness, this article argues that both hardness and Young's modulus are superior predictors of microscopic fracture toughness of rocks or minerals.

4.2 Connection between indentation morphology and micro-mechanical parameters

Typical indentation matrix morphology maps were chosen to assess the variability of mineral indentation morphology features in different parts of granite B before and after microwave action. Regarding the residual indentation area, it is consistent with the pattern presented by the residual depth in Section 3.4.1. As shown in Fig. 11, the residual indentation area of Q is the smallest, and the residual indentation areas of Afs and Pl are slightly larger, which implies that the three minerals have better mechanical properties and elastic recovery ability; the residual indentation area of Bit is the largest because Bit specifically has the poorest mechanical properties and the best plastic deformation ability. Similar conclusions have been drawn by Lei et al. (2021). After microwave irradiation, the change in the residual indentation area of Q is not significant, and there exists a small increase in the residual indentation area of Afs and Pl, which is related to the decrease in their elastic recovery ability. The indentation area of Bit is significantly increased, especially in the interior sample. In addition to the increase in plastic deformation capacity, this is also linked to the severe cracking and "chip dropping" phenomenon of Bit.

Therefore, importance should also be attached to the crack initiation and indentation integrity. Three typical cracking patterns can be observed in indentations, as summarized by Liu et al. (2022), namely lateral cracking, radial cracking and shear cracking. The authors believe that these can be linked to the mechanical properties and micro-structural features of the minerals. Before microwave irradiation, in the indentations of Q, Afs and Pl, only radial cracks existed in individual indentation points, so their indentation curves were quite smooth and perfect; whereas there were obvious combinations of radial cracks, shear cracks and isolated lateral cracks near the indentation points of Bit, which made the indentation morphology of Bit ill-defined and incomplete. Meanwhile, the presence of radial cracks and shear cracks rendered the load-depth curve of Bit to have obvious "pop-in" events and anomalous changes in slope, and these behaviors are related to the micro-structure of the contact region (Liu et al., 2022). After microwave irradiation, the radial cracks near the Q indentation remained insignificant, whereas radial crack lengths near the indentations of Afs and Pl increased considerably, especially in the interior sample. The authors attribute this phenomenon to the high fracture toughness of Q, Afs and Pl, but a marked decrease in the fracture toughness of Afs and Pl occurred after microwave irradiation. This was accompanied by the development of individual lateral cracks, which are mainly influenced by the presence of natural defects near the contact region (Liu et al., 2022). On the other hand, due to the decrease in fracture toughness, the crack length in Bit increased dramatically and was larger for the interior sample. It is worth noting that the extension direction of radial and shear cracks in Bit is heavily influenced by its laminate structure, as shown in Fig. 11, where cracks extend along the laminate direction at the top corners and side edges of the Bit's triangular indentation.

Furthermore, the indentation integrity is also affected by the phenomenon of chip-dropping near the indentation. The generation of chips, on the one hand, is because brittle minerals (Q, Afs and Pl) are prone to the formation of radial and lateral cracks in the deformation zone during indentation tests. When the lateral cracks join with the radial cracks, this leads to the phenomenon of chips in brittle minerals (Liu et al., 2022). Due to the high fracture toughness of these three minerals before microwave irradiation, the radial cracks were not obvious; this chip generation occurred mainly in Afs and Pl of the surface and interior sample after microwave irradiation. On the other hand, due to the weaker interlayer interaction and special laminate structure, the generation and extension of cracks caused by the indenter penetration into the Bit disintegrated surface also contribute to chip formation. This is the major reason why flaky chip spalling also occurred in Bit with low brittleness. At the same time, flaky chip spalling was more likely to occur in the Bit of the interior sample, which suggests that the reduction in mechanical properties contributes to the generation of this type of chips.

For the mineral interfaces, the indentations of Q-Afs and Q-Pl were relatively complete and had similar variation patterns of indentation morphology with Q, Afs and Pl after microwave irradiation, as seen in Fig. 11. On the contrary, the indentations

Table 1. Comparison of multiple upscaling results with uniaxial compression test results for granite B (the detailed derivation processes for the four upscaling models are shown in Appendix A).

Uniaxial compression test		Self-consistent method			Voigt-reuss-hill method			Mori-tanaka method			Generalized means method		
UT	MT	Unt	Sur	Int	Unt	Sur	Int	Unt	Sur	Int	Unt	Sur	Int
71.62	61.78	84.20	68.43	66.58	83.45	67.90	65.99	82.63	67.04	64.95	59.81	48.76	44.04

of Afs-Bit and Pl-Bit easily induced radial cracks along the interface direction, which was attributed by Liu et al. (2022) to stress concentration and uncoordinated deformation between hard and soft minerals. After microwave irradiation, the length of radial cracks on Afs-Bit and Pl-Bit increased, accompanied by the phenomenon of falling pieces from the Bit boundary.

4.3 Comparison of macro-mechanical test and upscaling results

For microwave-untreated granite B, the prediction errors of macro-modulus by the four upscaling methods were 17.56%, 16.52%, 15.37%, and 16.49%, respectively, compared with the results of uniaxial compression tests. As shown in Table 1, it can be seen that Mori-tanaka method (M-T) is the best method for predicting the macro-modulus of untreated granite. This is because it takes into account the interactions between pores and inclusions in the material. However, the homogenization results by the Mori-Tanaka method also have some bias. The reason is that the method is based on the assumption of isotropy and cannot reflect the anisotropic characteristics (Chen et al., 2023). Interestingly, among the other three methods, the error rates of the interior sample were generally 2%-3% lower than those of the surface sample, suggesting that the upscaling results of the interior sample are closer to those of the uniaxial compression tests. Meanwhile, the M-T method is still the best predictor of macro-modulus.

Another noteworthy phenomenon is that the values predicted by the Generalized means method were smaller than the experimental values, which is in line with the trend of deviation in the predictions of a wide range of granites, as counted by Ayatollahi et al. (2020). However, the predictions of the Self-consistent method, the Voigt-reuss-hill method and the M-T method are all heavily biased. The authors suggest three main reasons for this (Lei et al., 2021; Zhao et al., 2024): (1) large-size samples from uniaxial compression experiments contain more defects, such as microcracks and micropores, which are more prone to expansion and penetration upon loading; (2) the shape, distribution and bonding effects of the actual mineral grains in the granite differ from the assumptions made by these homogenization methods; and (3) the indenter is subjected to the squeezing effect of the surrounding minerals when pressed into it, and thus the indentation test-obtained micro-modulus is equivalent to the macro-modulus measured in the macro-mechanical tests under the condition of surrounding pressure.

5. Conclusions

This study mainly examined both the evolution and correlation of macro- and micro-mechanical parameters in a typical granite before and after microwave irradiation. The specific findings are outlined below:

The average surface heating rate of granite under 2 kW microwave irradiation was only 1.32 °C/s and no macroscopic damage was observed. The evaporation of various forms of water accelerated the granite mass decrease rate after the maximum surface temperature exceeded 200 °C. Meanwhile, B exhibited different weakening degrees of the various macro-mechanical parameters tested in uniaxial compression experiments. On a microscopic scale, independent of the minerals' microwave sensitivity, the mechanical parameters of Afs and Pl in the surface sample showed a higher folding rate. The parameter folding rates of Afs-Pl and Q-Bit were higher for the surface sample mineral interfaces, and the correlation between the interface mechanical properties and the mechanical properties of their neighboring minerals was weaker. It is reasonable to conclude that the micromechanical parameters of minerals and mineral interfaces of interior samples were further weakened to various degrees.

Indentation depth, creep displacement and residual depth are negatively correlated with hardness, but the laminar structure of Bit notably affected the latter two. Meanwhile, both hardness and Young's modulus are considered as excellent predictors of micro-fracture toughness. Residual indentation morphology is mainly characterized by the residual depth, fracture toughness, brittleness and microstructure of the minerals. For upscaling, the M-T method produces the best prediction effect on the macro-mechanical parameters of granite before and after microwave irradiation, especially using a pretreated interior sample.

Additional information: Author's email

zy0501a@163.com (Y. Zhang).

Conflict of interest

The authors declare no competing interest.

References

Ante, M. A., Lingareddy, M. G., Aminzadeh, F., et al. Nano- and micro-scale deformation behavior of sandstone and shale. Paper ARMA-2018-2055 Presented at 52nd U.S. Rock Mechanics/Geomechanics Symposium, Seattle, Washington, 17-20 June, 2018.

Ayatollahi, M., Najafabadi, M. Z., Koloor, S., et al. Mechanical characterization of heterogeneous polycrystalline rocks using nanoindentation method in combination with generalized means method. Journal of Mechanics, 2020, 36(6): 813-823.

Brady, B., Brown, E. Rock Mechanics: For Underground Mining. Dordrecht, Netherlands, Springer Dordrecht, 2007.

Broz, M. E., Cook, R. F., Whitney, D. L. Microhardness, toughness, and modulus of Mohs scale minerals. American Mineralogist, 2006, 91(1): 135-142.

BS EN ISO 14577-1:2002: Metallic materials. Instrumented indentation test for hardness and materials parameters: Test method. British Standards Institute, 2003.

Cheng, Y., Li, Z., Cheng, C. Scaling, relationships for indentation measurements. Philosophical Magazine A, 2002, 82(10): 1821-1829.

Chen, X., Cheng, Y., Xie, X., et al. Correlation between macro and micro mechanical parameters of marble based on nanoindentation experiment. Rock and Soil Mechanics, 2023, 44(12): 3551-3564.

Espinoza, W. F., Zhang, F., Dai, S. Impacts of temperature on the mechanical properties of Longmaxi shale outcrops using instrumented nanoindentation. Geomechanics for Energy and the Environment, 2022, 30: 100348.

Hartlieb, P., Grafe, B. Experimental study on microwave assisted hard rock cutting of granite. BHM Berg-und Hüttenmännische Monatshefte, 2017, 162(2): 77-81.

Hay, J. Introduction to instrumented indentation testing. Experimental Techniques, 2009, 33(6): 66-72.

Hertz, H. On the contact of elastic solids. Crelle's Journal, 1881, 92: 156-171.

He, X., Xu, Y., Shen, S., et al. Geological environment problems during metro shield tunnelling in Shenzhen, China. Arabian Journal of Geosciences, 2020, 13(2): 87.

Hill, R. The elastic behaviour of a crystalline aggregate. Proceedings of the Physical Society Section A, 1952, 65(5): 349-354.

Jerby, E., Aktushev, O., Dikhtyar, V. Theoretical analysis of the microwave-drill near-field localized heating effect. Journal of Applied Physics, 2005, 97(3): 034909.

Ji, S., Wang, Q., Xia, B., et al. Mechanical properties of multiphase materials and rocks: A phenomenological approach using generalized means. Journal of Structural Geology, 2004, 26(8): 1377-1390.

Kahraman, S., Canpolat, A. N., Fener, M., et al. The assessment of the factors affecting the microwave heating of magmatic rocks. Geomechanics and Geophysics for Geo-Energy and Geo-Resources, 2020, 6(4): 66.

Law, R. D. Deformation thermometry based on quartz c-axis

fabrics and recrystallization microstructures: A review. Journal of structural Geology, 2014, 66: 129-161.

Lei, M. Study on the meso-mechanical properties and mechanism of granite under combined action of hydrochemistry and freeze-thaw cycle based on nanoindentation test. Shaanxi, Xi'an University of Technology, 2022. (in Chinese)

Lei, M., Dang, F., Xue, H., et al. Evaluation method of granite multiscale mechanical properties based on nanoindentation technology. Geofluids, 2021, 2021: 1-9.

Li, C., Wang, D., Kong, L. Mechanical response of the Middle Bakken rocks under triaxial compressive test and nanoindentation. International Journal of Rock Mechanics and Mining Sciences, 2021, 139(7): 104660.

Liu, X., Xu, D., Li, S., et al. An insight into the mechanical and fracture characterization of minerals and mineral interfaces in granite using nanoindentation and micro X-Ray computed tomography. Rock Mechanics and Rock Engineering, 2023, 56(5): 3359-3375.

Liu, Y., Liu, A., Liu, S., et al. Nano-scale mechanical properties of constituent minerals in shales investigated by combined nanoindentation statistical analyses and SEM-EDS-XRD techniques. International Journal of Rock Mechanics and Mining Sciences, 2022, 159: 105187.

Lu, G., Feng, X., Li, Y., et al. The microwave-induced fracturing of hard rock. Rock Mechanics and Rock Engineering, 2019, 52: 3017-3032.

Lu, G., Li, Y., Hassani, F., et al. The influence of microwave irradiation on thermal properties of main rock-forming minerals. Applied Thermal Engineering, 2017, 112: 1523-1532.

Lu, G., Zhou, J., Li, Y., et al. The influence of minerals on the mechanism of microwave-induced fracturing of rocks. Journal of Applied Geophysics, 2020, 180: 104123.

Maruvanchery, V., Kim, E. Mechanical characterization of thermally treated calcite-cemented sandstone using nanoindentation, scanning electron microscopy and automated mineralogy. International Journal of Rock Mechanics and Mining Sciences, 2020, 125: 104158.

Mavko, G., Mukerji, T., Dvorkin, J. The Rock Physics Handbook. Cambridge, United Kingdom, Cambridge University Press, 2020.

Ma, Z., Gamage, R. P., Zhang, C. Application of nanoindentation technology in rocks: A review. Geomechanics and Geophysics for Geo-Energy and Geo-Resources, 2020, 6(4): 1-27.

Ma, Z., Zhang, C., Gamage, R. P., et al. Uncovering the creep deformation mechanism of rock-forming minerals using nanoindentation. International Journal of Mining Science and Technology, 2022, 32(2): 283-294.

Meng, Y. Processibility evaluation of granite based on micro-mechanical properties of rock-forming minerals. Fujian, Huaqiao University, 2022. (in Chinese)

Mori, T., Tanaka, K. Average stress in matrix and average elastic energy of materials with misfitting inclusions. Acta Metallurgica, 1973, 21(5): 571-574.

Mukherjee, R., Misra, S. Nanomechanics of minerals: Understandings and developments through instrumented

nanoindentation techniques. Physics and Chemistry of Minerals, 2023, 50(1): 10.

Nicco, M., Holley, E. A., Hartlieb, P., et al. Methods for characterizing cracks induced in rock. Rock Mechanics and Rock Engineering, 2018, 51(7): 2075-2093.

Nicco, M., Holley, E. A., Hartlieb, P., et al. Textural and mineralogical controls on microwave-induced cracking in granites. Rock Mechanics and Rock Engineering, 2020, 53(10): 4745-4765.

Oliver, W. C., Pharr, G. M. An improved technique for determining hardness and elastic modulus using load and displacement sensing indentation experiments. Journal of Materials Research, 1992, 7(6): 1564-1583.

Reuss, A. Berechnung der fließgrenze von mischkristallen auf grund der plastizitätsbedingung für einkristalle. ZAMM-Zeitschrift fur Angewandte Mathematik und Mechanik, 1929, 9(1): 49-58.

Róański, A., Róańska, A., Sobótka, M., et al. Identification of changes in mechanical properties of sandstone subjected to high temperature: Meso-and micro-scale testing and analysis. Archives of Civil and Mechanical Engineering, 2021, 21(1): 28.

Rui, F., Zhao, G., Zheng, Y., et al. Electromagnetic-thermo-mechanical coupled modelling of microwave-assisted TBM disc cutting. Tunnelling and Underground Space Technology, 2023, 138: 105171.

Rui, F., Zhao, G., Zhang, Y., et al. Study on the mechanism of rock damage under microwave and laser irradiation through multiscale and multiphysics numerical modelling. Rock Mechanics and Rock Engineering, 2024, 57(2): 1079-1102.

Sousa, F. J. P., Dal Bó, M., Guglielmi, P. O., et al. Characterization of Young's modulus and fracture toughness of albite glass by different techniques. Ceramics International, 2014, 40(7): 10893-10899.

Su, X., Li, D., Zhou, A., et al. Experimental studies on mechanical properties and brittleness of granite treated with different microwave heating times. Journal of Central South University, 2023, 30(12): 4052-4065.

Swan, G. The mechanical properties of Stripa granite.

Lawrence Berkeley National Laboratory, 1978.

Tang, X., Zhang, Y., Xu, J., et al. Determining Young's modulus of granite using accurate grain-based modeling with microscale rock mechanical experiments. International Journal of Rock Mechanics and Mining Sciences, 2022, 157: 105167.

Voigt, W. Lehrbuch der Kristallphysik. Leipzig, DE, Teubuer, 1928.

Wong, L. N. Y., Zhang, Y., Wu, Z. Rock strengthening or weakening upon heating in the mild temperature range? Engineering Geology, 2020, 272: 105619.

Xie, H., Gao, M., Zhang, R., et al. Application prospects of deep in-situ condition-preserved coring and testing systems. Advances in Geo-Energy Research, 2024, 14(1): 12-24.

Yang, M., Li, J., Gao, M., et al. Experimental study on nonlinear mechanical behavior and sampling damage characteristics of rocks from depths of 4900-6830 m in Well Songke-2. Journal of Central South University, 2023, 30(4): 1296-1310.

Yang, Z., Pan, D., Zhou, J., et al. Vibration characteristics of cutter-head in soft-hard mixed stratum: An experimental case study on Su'ai tunnel. KSCE Journal of Civil Engineering, 2020, 24(4): 1338-1347.

You, M., Hua, A. Fracture of rock specimen and decrement of bearing capacity in uniaxial compression. Chinese Journal of Rock Mechanics and Engineering, 1998, 17(3): 292-296.

Zhang, J., Hu, L., Pant, R., et al. Effects of interlayer interactions on the nanoindentation behavior and hardness of 2:1 phyllosilicates. Applied Clay Science, 2013, 80-81: 267-280.

Zhao, L., Peng, R., Hao, P., et al. Effects of pore pressure on coring-induced damage based on simulation by mesoscale stress-flow coupling numerical model. Advances in Geo-Energy Research, 2024, 14(3): 170-186.

Zhu, W., Hughes, J. J., Bicanic, N., et al. Nanoindentation mapping of mechanical properties of cement paste and natural rocks. Materials Characterization, 2007, 58(11-12): 1189-1198.

Appendix A. Calculation of macro-mechanical parameters

In addition to easily measurable parameters such as peak strength and peak strain, other macro-mechanical parameters can be derived from the stress-strain curve characteristics to investigate the impact of microwave treatment on the mechanical properties of granite. The mid-body strain is calculated as follows (Brady and Brown, 2007):

$$\varepsilon_v = \varepsilon_1 + 2\varepsilon_3 \tag{A1}$$

where ε_v represents the volumetric strain; ε_1 represents the axial strain; ε_3 represents the circumferential strain. In addition, the elastic modulus and Poisson's ratio of rocks can be calculated as follows (Brady and Brown, 2007):

$$E = \frac{\sigma_b - \sigma_a}{\varepsilon_b - \varepsilon_a}, \qquad \upsilon = \frac{\varepsilon_{dp}}{\varepsilon_{lp}} \tag{A2}$$

where σ_a, σ_b represent the starting and ending stress values of the straight line segment in the stress-strain curve, respectively, MPa; ε_a, ε_b represent the starting and ending strain values of the straight line segment in the stress-strain curve, respectively; ε_{dp}, ε_{dp} represent the average values of the strain in the corresponding straight line segment portion on the stress-annular strain curve and stress-axial strain curve, respectively.

Appendix B. Calculation of micro-mechanical parameters

The Oliver-Pharr method is a commonly utilized international analytical technique for determining micro-mechanical parameters such as hardness and Young's modulus at the maximum indentation depth.

The contact stiffness is specified as the slope of the tangent line at the maximum load on the unloading curve, and it can be expressed as:

$$S = \frac{dP}{dh}\big|_{h=h_m} \tag{A3}$$

The reduced modulus is calculated as:

$$E_r = \frac{\sqrt{\pi}}{2\beta}\frac{S}{\sqrt{A_c}} \tag{A4}$$

The contact area A_c is related to the contact depth h_c, which can be expressed as:

$$A_c = f(h_c) \tag{A5}$$

For the Berkovich indenter, the contact depth can be expressed as:

$$h_c = h_m - \varepsilon\frac{P_m}{S} \tag{A6}$$

Hardness is calculated as:

$$H = \frac{P_m}{A_c} \tag{A7}$$

According to the Hertz contact theory (Hertz, 1881), the Young's modulus of a material can be calculated as follows:

$$E = \left(1 - v^2\right)\left(\frac{1}{E_r} - \frac{1 - v_i^2}{E_i}\right)^{-1} \tag{A8}$$

where β represents the indenter correction factor and ε is a constant related to the shape of the indenter. For the Berkovich indenter, $\beta = 1.034$ and $\varepsilon = 0.75$. Among the parameters, h_c denotes the contact depth; A_c denotes the contact area that can be expressed as $A_c = 24.56h_c^2$ (Oliver and Pharr, 1992); E_r is the reduced modulus, which represents the interaction effect between the indenter and the material; E_i and v_i denote the Young's modulus and Poisson's ratio of the indenter, respectively. For the diamond indenter used in this study, $E_i = 1141$ GPa and $v_i = 0.07$. v is the Poisson's ratio of the indented material. This can be reasonably assumed based on the relevant literature (Mavko et al., 2020). The explanation is that a sensitivity analysis of the Poisson's ratio with 40% uncertainty shows that the uncertainty in Young's modulus is only 5% (Hay, 2009).

Appendix C. Micro-fracture toughness calculation

The authors chose the energy analysis method (Cheng et al., 2002) to calculate fracture toughness, which obtains this parameter simply on the basis of the single load-displacement curve of the nanoindentation. During nanoindentation, the total energy (U) is composed of two elements: elastic energy (U_e) and plastic energy (U_p). The plastic energy (U_p) in turn consists of two elements: induced fracture energy (U_{frac}) and pure plastic energy (U_{pp}). The specific energy balance equation is expressed as follows (Cheng et al., 2002; Ma et al., 2020):

$$U = U_e + U_p = U_e + U_{pp} + U_{frac} \tag{A9}$$

where U and U_e can be gained by integrating the loading and unloading curves over the load-displacement curve.

According to the linear elastic fracture mechanics, the fracture toughness K_{IC} can be calculated for plane strain conditions (described below):

$$K_{IC} = \sqrt{G_c E_r \left(1 - v^2\right)} \tag{A10}$$

This equation applies to thick boards, such as rocks and minerals, where the constraining effect of deformation in the thickness direction results in no strain in the z direction, i.e., $\varepsilon_z = 0$. This state, where strain exists in only two directions, is called the plane strain case. Here, E_r represents the reduced modulus and G_c represents the strain energy release rate. G_c can be calculated by:

$$G_c = \frac{\partial U_{frac}}{\partial A_c} = \frac{U_{frac}}{A_c} \tag{A11}$$

where A_c represents the projection contact area and U_{frac} can be calculated from Equation (10), expressed as:

$$U_{frac} = U_p - U_{pp} = U - U_e - U_{pp} \tag{A12}$$

Although U and U_e are known, U_{pp} cannot be directly determined from curves but it is typically obtained through a combination of experimental and finite element simulation results. According to Cheng et al. (2002), U_{pp} can be expressed as:

$$U_{pp} = \left\{ 1 - \left[\frac{1 - 3\left(\frac{h_f}{h_{\max}}\right)^2 + 2\left(\frac{h_f}{h_{\max}}\right)^3}{1 - \left(\frac{h_f}{h_{\max}}\right)^2} \right] \right\} U \tag{A13}$$

The fracture toughness can be obtained by substituting it into Eqs. (A12), (A11), and (A10) sequentially. In this process, it is not necessary to measure the length of the crack.

Appendix D. Upscaling calculation

(1) Self-Consistent method

On the basis of the equilibrium of strain energy stored or dissipated by the material over a certain volume range, the Self-Consistent method (S-C method) replaces anisotropic composites with an idealized homogeneous continuum. The mechanical behavior of the two media is the same when the scale range is much larger than the local characteristic dimensions of the anisotropic material. The effective modulus of the composite material can be expressed as follows:

$$\overline{C} = C_0 + \sum_{r=1}^{N-1} c_r (C_r - C_0) \left[I + \overline{P}_r (C_r - \overline{C}) \right]^{-1} \tag{A14}$$

where C_0 and C_r represent the modulus of the mineral with the largest content and the modulus of the rth phase mineral, respectively; c_r represents the volume fraction of phase r; I represents a tensor related to the inclusions' shape; $\overline{P}_r$ represents the P tensor when the phase r is placed in an unknown composite material used as a matrix. $\overline{P}_r$ is related to the shape of the inclusions and the modulus of the unknown composite $\overline{C}$. The above is the implicit equation for the effective modulus of the composite.

By using a simplified algorithm for the isotropic tensor, implicit equations for the effective shear modulus and bulk modulus of granite were obtained (Lei et al., 2021):

$$\begin{cases} G^{hom} = \sum_{r=0} c_r \dfrac{5G_r \cdot G^{hom} \left(3K^{hom} + 4G^{hom}\right)}{G^{hom} \left(9K^{hom} + 8G^{hom}\right) + 6G_r \left(K^{hom} + 2G^{hom}\right)} \\[3mm] K^{hom} = \sum_{r=0} c_r \dfrac{K_r \left(3K^{hom} + 4G^{hom}\right)}{3K_r + 4G^{hom}} \end{cases} \tag{A15}$$

where G^{hom} and K^{hom} denote the effective shear modulus and bulk modulus of the homogenized granite, respectively; G_r and K_r are the shear modulus and bulk modulus of phase r, respectively. The calculation equation is as follows:

$$G_r = \frac{E}{2(1+v)}, \qquad K_r = \frac{E}{3(1-2v)} \tag{A16}$$

(2) Voigt-Reuss-Hill method

The Voigt-Reuss-Hill method (V-R-H method) takes into account the link between the elastic behavior of aggregates and single crystals. Therein, the Voigt boundaries (upper boundaries) and Reuss boundaries (lower boundaries) are the average elastic properties of multiphase and polycrystalline aggregates, respectively (Hill, 1952). The average values provide a convenient way of estimating the rock properties of aggregates, without considering the orientation and interlocking of the particles.

The upper bound of the equivalent modulus for the n components is derived from the Voigt model (Voigt, 1928):

$$M_v = \sum_{i=1}^{n} \varphi_i M_i \tag{A17}$$

where φ_i and M_i represent the volume content and Young's modulus of the ith component, respectively. The Voigt model assumes that the components are isotropic and linearly elastic.

The lower bound of the equivalent modulus for the n components is derived from the Reuss model (Reuss, 1929):

$$\frac{1}{M_{\mathbb{R}}} = \sum_{i=1}^{n} \frac{\varphi_i}{M_i} \tag{A18}$$

The Hill model (Hill, 1952) uses the average of the upper and lower boundaries to calculate the equivalent modulus:

$$M = \frac{1}{2}(M_v + M_R) \tag{A19}$$

(3) Mori-Tanaka method

The Mori-Tanaka method (M-T method), proposed by Mori and Tanaka in 1973 (Mori and Tanaka, 1973), takes into account the interactions between inclusions and assumes that each inclusion is embedded in an infinitely large matrix. The
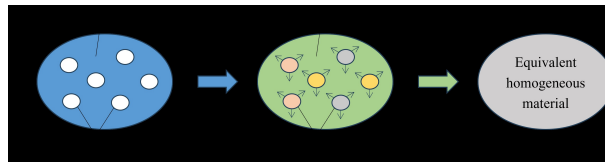
Fig. A1. Homogenization process of the M-T method.

homogenization process of the method is shown in Fig. A1. The effective modulus of the composite material can be expressed as follows:

$$\overline{C} = C_0 + \sum_{r=1}^{N-1} c_r \left[(C_r - C_0)^{-1} + c_0 P_r \right]^{-1}$$

(A20)

The bulk and shear modulus of granite are expressed as follows:

$$
\begin{cases}
G^{hom} = \dfrac{\sum\limits_{r=0} \dfrac{c_r G_r}{G_0(9K_0+8G_0)+6G_r(K_0+2G_0)}}{\sum\limits_{r=0} \dfrac{c_r}{G_0(9K_0+8G_0)+6G_r(K_0+2G_0)}} \\[20pt]
K^{hom} = \dfrac{\sum\limits_{r=0} \dfrac{c_r K_r}{3K_r+4G_0}}{\sum\limits_{r=0} \dfrac{c_r}{3K_r+4G_0}}
\end{cases}
$$

(A21)

where K_0 and G_0 denote the bulk and shear modulus of Bit, respectively. Considering the obvious pore structure of Bit, the bulk modulus and shear modulus of Bit are expressed as follows:

$$
\begin{cases}
G_0 = \dfrac{(1-\varphi)\,G_s}{1+6\varphi\frac{K_s+2G_s}{9K_s+8G_s}} \\[14pt]
K_0 = \dfrac{4\,(1-\varphi)\,K_s G_s}{4G_s+3\varphi K_s}
\end{cases}
$$

(A22)

where K_s and G_s represent the bulk modulus and shear modulus of Bit, respectively, independent of the pore structure; φ is the porosity of Bit. Considering the special laminar structure of Bit, this study set the percentage of pore volume in Bit to the total volume to 30%.

(4) Generalized Means method

The Generalized Means method (G-M method) is a semi-empirical model for predicting the mechanical properties of multiphase materials and polycrystalline rocks (Ji et al., 2004). The mechanical properties of multiphase materials in the G-M method are related to the volume fraction and composition of the material, which can be determined by the following equation (Ayatollahi et al., 2020; Ji et al., 2004):

$$M_d(J) = \left[\sum_{i=1}^{n} \left(f_i M_i^J \right) \right]^{1/J}$$

(A23)

$$\sum_{i=1}^{n} f_i = 1$$

(A24)

where the subscripts i and d stand for the ith phase and the multiphase material consisting of n phases, respectively; f_i denotes the volume fraction of each phase; M is a certain mechanical property; and J is the mesostructure coefficient, whose value depends on the mesostructure.

Note that the value of J for each multiphase material must be measured separately by multiple tests. For polycrystalline rocks (e.g., granite), Ayatollahi et al. (2020) found that the predicted Young's modulus matches very well with the results of uniaxial compression tests when J is infinitesimal. On the other hand, the predicted Young's modulus values are almost constant when J is beyond the range of (-50,50). Therefore, the authors chose $J = $ -50 as the J value for the predicted modulus.

For the equivalent mechanical parameters of the four types of mineral media obtained by using the S-C and M-T methods, on the basis of the theory of elastic mechanics, the Young's modulus of the rock at the centimeter scale can be calculated using Eq. (A25):

$$E^{hom} = \frac{9K^{hom} \cdot G^{hom}}{3K^{hom} + G^{hom}}$$

(A25)